Research Article | Vol. 29, No. 6 / 15 March 2021 / Optics Express 7956
Optics EXPRESS

Waveguide integrated hot electron bolometer for classical and quantum photonics

F. MARTINI,* S. CIBELLA, A. GAGGERO, F. MATTIOLI, AND R. LEONI

Istituto di Fotonica e Nanotecnologie - CNR, Via Cineto Romano 42, 00156 Roma, Italy
**francesco.martini@ifn.cnr.it*

Abstract: The development of performant integrated detectors, which are sensitive to quantum fluctuations of coherent light, are strongly desired to realize a scalable and determinist photonic quantum processor based on continuous variables states of light. Here, we investigate the performance of hot electron bolometers (HEBs) fabricated on top of a silicon-on-insulator (SOI) photonic circuit showing responsivities up to 8600 V/W and a record noise equivalent temperature of 1.1 dB above the quantum limit. Thanks to a detailed analysis of the noise sources of the waveguide integrated HEB, we estimate 14.8 dBV clearance between the shot noise and electrical noise with just 1.1μW of local oscillator power. The full technology compatibility with superconducting nanowire single photon detectors (SNSPDs) opens the possibility of nonclassical state engineering and state tomography performed within the same platform, enabling a new class of optical quantum processors.

1. Introduction

Shot-noise limited (SNL) photodetectors are able to observe the quantum fluctuation of light arising from the discretized nature of coherent beams. In a homodyne detection, SNL detectors are used to characterize quantum states [1–3], finding application in continuous variable (CV) quantum information processing [4], quantum key distribution [5] and quantum metrology [6]. Unlike the use of photons for quantum technologies, the use of CV degree of freedom to encode quantum information holds the advantage of a deterministic generation of quantum states and operations, allowing the production of large-scale cluster states [7], although non-Gaussian operations are required to achieve universal quantum computation.

The quest to enlarge the capabilities of quantum information experiments based on non-classical states of light has directed the research toward an integrated approach [8]. Thanks to the miniaturization provided by photonic integrated circuits (PICs), quantum states could be efficiently generated, interfere and be detected within the same integrated circuit. Several advantages come from the integration of CV experiments, ranging from system stability to ideal mode overlaps between waveguides [9–11]. The high confinement experienced in guided structures enhances the nonlinear effects required to squeeze the field quadratures and consequently high-squeezing level can be reached with single-pass waveguide [12,13], without the use of phase locked cavities. This is also crucial to generate squeezed states with a THz bandwidth [12,14], essential for quantum information processing using time-domain multiplexing scheme [15]. Different material platforms have been employed to generate CV states in integrated structures ranging from second-order nonlinear materials (periodically poled $LiNbO_3$ [10,12,16] and $KTiOPO_4$ [17]) to the low-loss CMOS-compatible Si_3N_4 [18,19].

Although the high squeezing level reached in waveguides, the scalability is hampered from the lack of on-chip detection on most optical platforms. Additionally, CV states suffer the losses encountered from the non-ideal coupling from waveguide to fiber (outcoupling losses) required to perform off-chip detection. Ideally [20], detectors should guarantee unity quantum efficiency, high bandwidth and be integrated on photonic materials generating high-squeezing levels. To

#410317 https://doi.org/10.1364/OE.410317
Journal © 2021 Received 15 Sep 2020; revised 16 Dec 2020; accepted 21 Dec 2020; published 1 Mar 2021

Optics EXPRESS

date, the only demonstration of on-chip tomography has been reported just on SOI technology [11], where the small lattice mismatch with germanium allows the heteroepitaxial growth of efficient photodetectors [21]. Even though hybrid technologies could be used to achieve on-chip detectors in other optical platform than silicon, it relies on die-to-wafer bonding process which complicates the fabrication procedure [22]. Photodetectors based on 2D materials, like graphene [23] or transition metal dichalcogenides [24], could be potentially integrated on every material platforms but suffer from low quantum efficiencies due to low absorption in atomically thin films.

Here, we propose the use of a HEB [25], made with niobium nitride (NbN), integrated in a waveguide as fundamental building block to implement on-chip state tomography. This detector exploits the steep change of resistance of a superconducting material when is close to its transition temperature T_C. Due to their large sensitivity and speed, HEBs have been the preferred choice for detecting light from mid-infrared [26] to THz spectral range [27,28]. The only demonstration of the use of a HEB to detect light at telecom wavelength was obtained by coupling the HEB with a single mode fiber [29,30]. NbN has been one of the most used active material for the fabrication of superconducting nanowire single photon detectors (SNSPDs) and the technological compatibility with several photonics platforms has already been proved in both CMOS materials [31–33] and $LiNbO_3$ [34], to name a few. The possibility to integrate homodyne detectors together with single photon detectors open the prospect for the on-chip generation and characterization of Schrödinger Kittens [3] and, more generally, to realize fault tolerant universal quantum computers [35].

In this work we integrate a HEB on a SOI PIC, showing a responsivity as high as 8600 V/W and allowing 14.8 dBV clearance between shot noise and electronic noise with just 1.11 μW of input power. Even though in our experiment we are limited by the 150 MHz bandwidth of the photodiode used for the calibration, the time constant of NbN HEBs is reported to be lower than 50ps, meaning that frequency bandwidths of 20 GHz are theoretically possible [25]. The development of a SNL detector which could be easily integrated with materials used to implement efficient squeezer represents a fundamental step toward the achievement of complete photonic platforms for large-scale quantum information processor with CVs state of light.

2. Fabrication and experimental setup

In order to fabricate a HEB integrated on a PIC, we start with the deposition of 6 nm-thick NbN film by DC magnetron sputtering on top of standard 220 nm-thick SOI wafer (BOX thickness 2μm). A first electron beam lithography defines the contact pads designed as a coplanar waveguide by using a lift-off process employing PMMA as stencil mask for the deposition of Ti/Au bilayer (thickness of 10nm/60nm, respectively). Successively, the superconducting active area is patterned using a 100nm-thick HSQ resist and a RIE etching step. More details on the fabrication procedure employed for the HEB can be found in Ref. [32] as it shares the same technological process with NbN SNSPDs. A last electron beam lithography step patterns the Si photonic layer using 400nm-thick CSAR as resist and a RIE etching. Finally, the residual CSAR is removed with a combination of O_2 plasma and ultrasonic cleaning prior to the spinning of 1μm-thick PMMA as top cladding. The 1×1 μm^2 HEB is positioned at the waveguide end as it is shown in the SEM micrograph of Fig. 1(a) and it is optically coupled via evanescent coupling to the 500nm-wide waveguide. The figure also shows the absorption profile simulated with a FDTD solver for the fabricated structure, providing a coupling efficiency of 57%. The refractive index for NbN used in the simulation is n_{NbN}=5.23+i5.82 meanwhile we employed 1.48 for the PMMA as cladding. As can be seen from Fig. 1(a) the absorption is maximum in the central area of the NbN and it decreases exponentially as the light propagates toward the border of the active area.

As the HEB works at temperatures below the critical temperature of the superconducting NbN thin film, the electro-optical characterization of the device requires that the fiber-grating optical links are preserved down to low temperatures. To achieve this, we first maximize the light coupled from the fiber array (FA) to the PIC at room temperature and then we glued it using

Optics EXPRESS

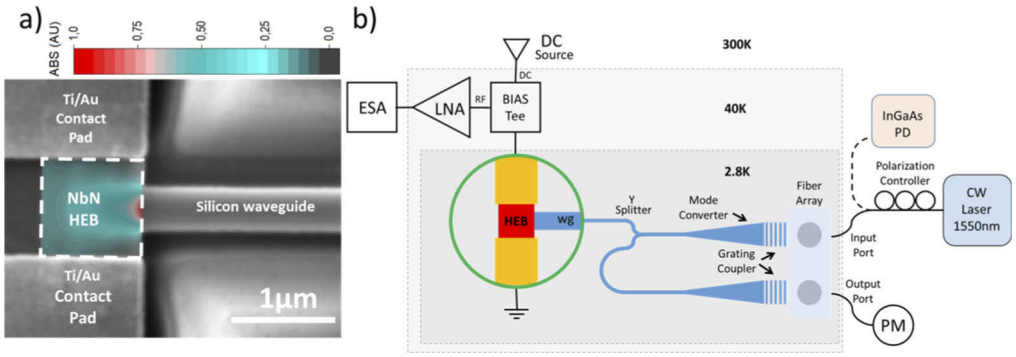

Fig. 1. (a) SEM micrograph of a 500nm-wide waveguide feeding light to the HEB together with the 1×1 µm^2 HEB detector, where the absorption profile is superimposed. (b) Experimental setup for the electro-optical characterization of the integrated HEB. Legend: PM power meter, PD photodiode, LNA low noise amplifier, ESA electronic spectrum analyser, HEB hot electron bolometer, WG waveguide.

a cyanoacrylate adhesive [32]. The device is successively mounted inside a GM closed-cycle refrigerator and cooled down to the base temperature of 2.8 K. The coupling efficiency of the grating drops from 1.37% (300 K) to 0.95% (2.8 K). Figure 1(b) shows the complete experimental setup employed for the electro-optical characterization of the integrated HEB. The light coming from a CW telecom laser is injected through the input port of the fiber array and coupled inside the PIC thanks to a grating coupler. The light power is divided in half by a Y splitter: one arm is used to feed the light to the HEB meanwhile the other arm is connected to the output port where a power meter (PM) monitors the light outcoupled by a second grating coupler. The coupling efficiency of the grating coupler is maximized thanks to a fiber polarization controller. From the electrical side, a bias tee is used to both bias the detector with a current generator and to extract the RF signal. This is amplified with a cryogenic low noise amplifier (LNA) [36], operating at 40 K, and successively measured with an electronic spectrum analyser (ESA). For comparison, the spectral properties of the light are also measured after the fiber polarization controller with an InGaAs photodiode (Thorlabs PDA05CF2).

3. Results

HEBs can be operated as a direct detector at temperatures on the edge of the superconducting to normal transition of the NbN film [27]. In this regime, a small change in temperature or absorbed power gives rise to a large variation in the HEB resistance. This effect is best exploited by choosing the bias point of the characteristic current-voltage (IV) curve where the dynamic resistance $R_d = \partial V/\partial I$ is maximum and continuous (to avoid instabilities in the HEB biasing and response) [37]. Figure 2(a) shows the IV curves for the fabricated HEB at different bath temperatures. The inset of Fig. 2(a) reports the resistance vs temperature characteristics, showing a critical temperature $T_C \backsimeq 6.5$ K.

HEBs can also be operated as a mixer, where a bias light source is employed to heat the electrons and set the operating IV characteristic while keeping the bath temperature at cryostat base temperature, 2.8 K in our case. In this configuration, HEBs can be operated together with SNSPDs, whose internal quantum efficiency is maximized at the cryostat base temperatures. Figure 2(b) shows the IVs for different light powers P_{HEB} impinging the HEB. By comparing the characteristics of both plots of Fig. 2, the bias resistance $R = V/I$ at $I \rightarrow 0$ is different in the two heating conditions. As a direct detector (Fig. 2(a)), where both electron and phonon temperatures are increased by the resistive heater, the resistance R $\backsimeq 50\ \Omega$ is given by the transition of the

Optics EXPRESS

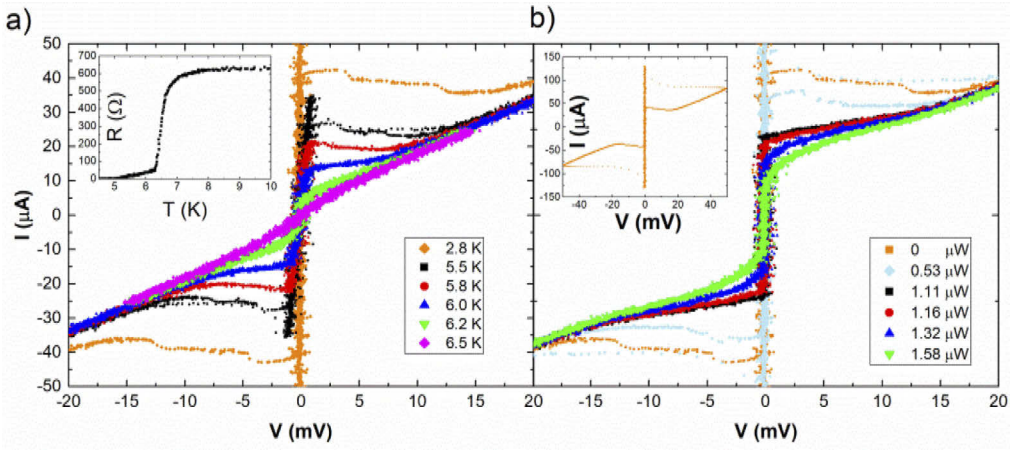

Fig. 2. Current versus voltage characteristics of the HEB in different heating conditions: (a) IVs for different bath temperatures T obtained by using a resistive heater placed underneath the sample holder; (b) IVs at different light power P_{HEB} at 1550 nm travelling in the waveguide and taken at bath temperature of 2.8 K. The inset of Fig. 2(a) shows the R vs T plot meanwhile the inset of Fig. 2(b) shows the complete IV characteristic at base temperature.

contacts whose proximity effect, due to the stack of NbN/Ti/Au layers, results in an additional transition temperature at ~5 K (inset of Fig. 2(a)). As a mixer (Fig. 2(b)), the photons fed by the waveguide, whose width is smaller compared to the side of the active area of the HEB, allow to locally increase the temperature of the electrons confined in the NbN active area leaving the phonons at bath temperature of 2.8 K. As a result, the static resistance R≃0 and the ratio R_d/R becomes very large providing a great improvement in the detector responsivity, as will be explained later.

Our goal is to demonstrate a shot-noise limited detector, in which all the sources of electronic noise (i.e. independent of light) are well below the noise deriving from quantum fluctuation of light. To achieve this, we illuminate the HEB with a CW laser source that not only sets the desired shape of the IV characteristic, but increases the noise level due to the shot noise. For light powers above 1.11μW the fabricated HEB has not discontinuities in the IV (Fig. 2(b)) and then it can be current-biased in each point of its characteristic.

Figure 3(a) shows the spectral properties of the absorbed light measured by the integrated HEB in two different conditions: i) P_{HEB}=1.11 μW and I_B = 20.5 μA (red curve), ii) P_{HEB}=1.58 μW and I_B=8 μA (blue curve). In both curves, the spectral signal is amplified by the LNA and the output is collected with the ESA. The spectral properties of the laser light are calibrated using the photodiode response illuminated with a 200 μW CW power (black curve). The peaks in the frequency response of both the HEB and the photodiode arise from the constructing interference of the light reflected from fiber flat tips of the fiber polarization controller, resulting in a cavity-like behaviour of free spectral range of ~16 MHz.

The responsivity of the HEB can be computed as $Resp(f)=V_{HEB}(f)/P_{IN}(f)$. The HEB voltage response $V_{HEB}(f)$ is derived from the HEB spectral response, i.e. red/blue curve of Fig. 3(a), divided by the LNA gain and normalized by the input power (1.11 μW and 1.58 μW, respectively). The spectral RF power $P_{IN}(f)$ is estimated from the photodiode response (black curve of Fig. 3(a)) using its responsivity, divided by the photodiode amplifier gain and normalizing by the input power (200 μW). Figure 3(b) shows the computed point-by-point responsivity for the HEB with P_{HEB} = 1.11 μW light power and polarized at I_B=20.5 μA (red curve). The responsivity is not constant and shows the same spectral peaks of Fig. 3(a). This is due to the presence of two sources

Optics EXPRESS

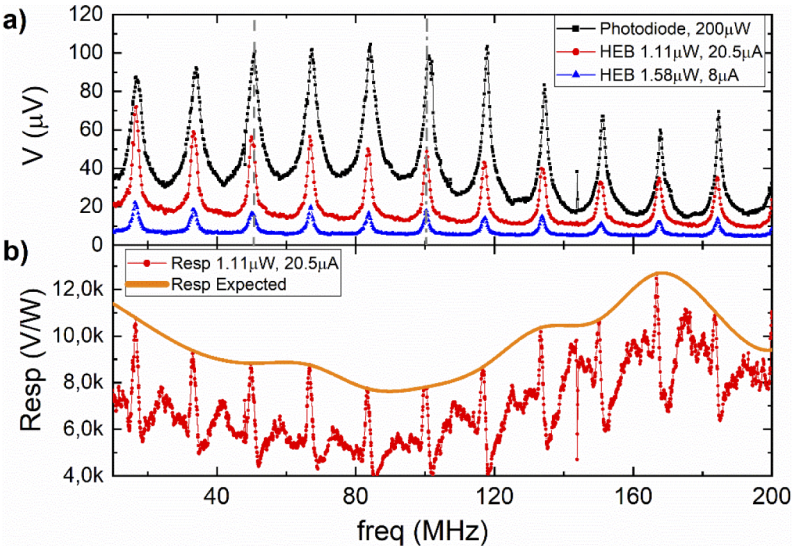

Fig. 3. (a) HEB spectral response as measured at the output of the LNA (gain of 37 dB) in two cases: i) I_B=20.5μA and P_{HEB}=1.11μW (red curve) and ii) I_B=8μA and P_{HEB}=1.58μW (blue curve). In both cases, the ESA resolution bandwidth is RBW=10 kHz and the video bandwidth is VBW=100 kHz. Spectral properties of the laser light (power of 200μW) measured with a photodiode (black curve), taken with RBW=10 kHz, VBW=1 kHz. (b) Responsivity of the HEB (I_B=20.5μA and $P_{HE}B$=1.11μW) computed for all the spectral points.

of optical noise that are affected differently by the light attenuation A: the shot noise, which scales as $A^{1/2}$, and the power fluctuation noise of the laser, that scales linearly as A [38]. $P_{IN}(f)$ is affected mainly by the latter meanwhile the voltage noise in the valley between two consecutive peaks is affected from the shot noise. As the voltage noise in the valley scales non-linearly with A, only the peaks are considered in the responsivity (orange curve of Fig. 3(b)). The non-flat response of the peaks is due to the non-flat gain of the LNA and the cut-off frequency of the photodiode (150 MHz), as HEBs have shown to have a bandwidth of several GHz [30].

Considering the peaks in the spectral response at 50 MHz and 100 MHz, Fig. 4 shows the responsivity values for different light power as a function of the polarization current. For low bias currents, the HEB is still superconductive and unable to respond to the light excitation. The HEB is instead completely resistive for high bias currents and the light affects slightly its resistance. The maximum voltage responsivity is obtained for bias currents where the dynamic resistance R_d of the IV characteristics is much larger than $R = V/I$ [39]

$$Resp = \frac{dV}{dP} = \frac{1}{2I_b} \cdot \frac{\frac{R_d}{R} - 1}{\frac{R_d}{Z_L} + 1} \tag{1}$$

where Z_L is the load resistance, typically 50Ω (given by input impedance of the cryogenic amplifier). The measured responsivity reach its maximum of 8600 V/W by polarizing the HEB at I_B = 20.5 μA and an illumination P_{HEB}=1.11 μW (Fig. 4 on the right). As the local oscillator power P_{HEB} increases, the responsivity peak occurs at lower bias currents and its maximum value decreases. Being the HEB a variable resistance of value R_d, it is possible to infer the current responsivity (measured in A/W) from the voltage responsivity (measured in V/W) as they are linked by the Ohm's Law. From the IV of Fig. 2(b), we can retrieve the $R_d \backsimeq 100$ Ω (see

Optics EXPRESS

Supplement 1) and consequently we would expect to measure a current responsivity of~ 86 A/W if we biased the HEB with a DC voltage source.

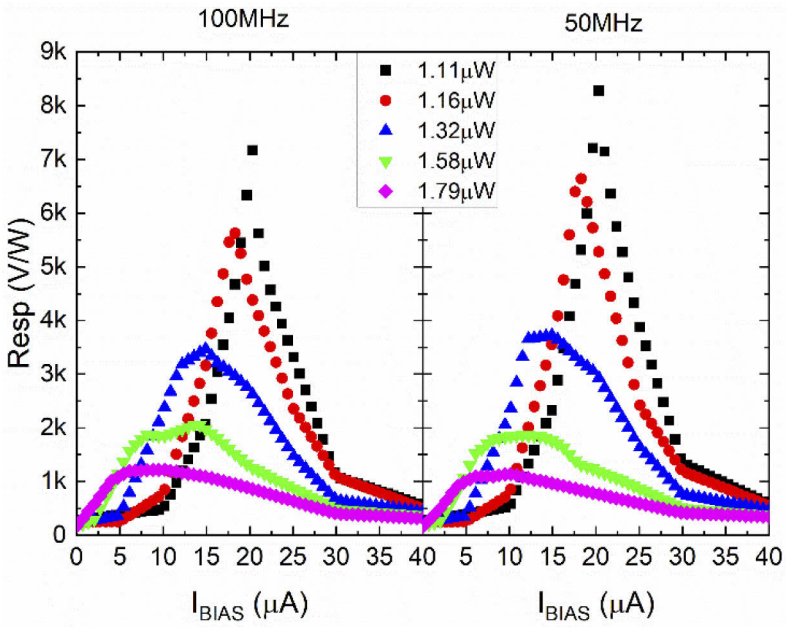

Fig. 4. HEB responsivities measured at 100 MHz and 50 MHz as a function of the bias current for different local oscillator powers.

4. Noise analysis

The sensitivity of HEBs is subjected to three electronic noise sources that are independent from the light [27,40]. Being the HEB a variable resistance, it is affected by the Johnson noise:

$$NEP_J^2 = \frac{4k_BT(R + 2R_d)}{Resp^2} \tag{2}$$

where k_B is the Boltzmann constant and T is the HEB operating temperature that in a first approximation is $\sim T_C$. The random exchange of energy between the thermal reservoir and the HEB causes the thermal fluctuation noise:

$$NEP_{th}^2 = 4k_BT^2G \tag{3}$$

with G the thermal conductance of the HEB at the operating temperature T. Finally, the input resistance of the amplifier R_{IN} at a temperature T_{AMP} generates also Johnson noise:

$$NEP_{AMP}^2 = \frac{4k_BT_{AMP}R_{IN}}{Resp^2} \tag{4}$$

As all the noise sources are independent from each other, the total electrical NEP_{EL} is given by

$$NEP_{EL} = \sqrt{NEP_{AMP}^2 + NEP_{th}^2 + NEP_J^2} \tag{5}$$

In order to have the HEB shot-noise limited, it is required that NEP_{EL} is much smaller than the quantum fluctuation noise power of the light

$$NEP_{SN} = \sqrt{2h\nu P_{HEB}} \tag{6}$$

Optics EXPRESS

with $h\nu$ the photon energy at 1550 nm wavelength. In our experimental setup, we have direct access to the voltage noise density $V_n(f)$ as measured at the output of the ESA that can be directly compared to the total $NEP_{tot} = \sqrt{NEP_{SN}^2 + NEP_{EL}^2}$, by multiplying it with the responsivity. Figure 5 shows the contour plot of the measured voltage noise at 90 MHz as function of the light power and the bias current. Three clear region can be identified. In the bottom left of the chart the voltage noise reach its minimum since only the electrical noise of the amplifier contributes (the HEB is superconductive and not responsive, so both Johnson noise and light noise does not affect V_n). The measured value $V_n = 0.27$ nV/Hz$^{1/2}$ is comparable to the expected value of $V_{n-AMP} = 0.33$ nV/ Hz$^{1/2}$ (from Eq. (4)). In the top right, the noise is mostly influenced by both the amplifier and the HEB Johnson noise (HEB is completely resistive and not responsive being $R_d/R \backsimeq 0$). The measured noise $V_n = 0.49$ nV/ Hz$^{1/2}$ is close to $V_{n-Res} = \sqrt{V_{n-AMP}^2 + V_{n-Norm}^2} = 0.51nV/ Hz^{1/2}$, where V_{n-Norm} is the Johnson noise contribution of the normal-state resistance (~500 Ω) at 6.5 K temperature. The middle region is where the HEB is responsive (being $R_d/R \gg 1$) and all noise sources, including the shot noise, are present.

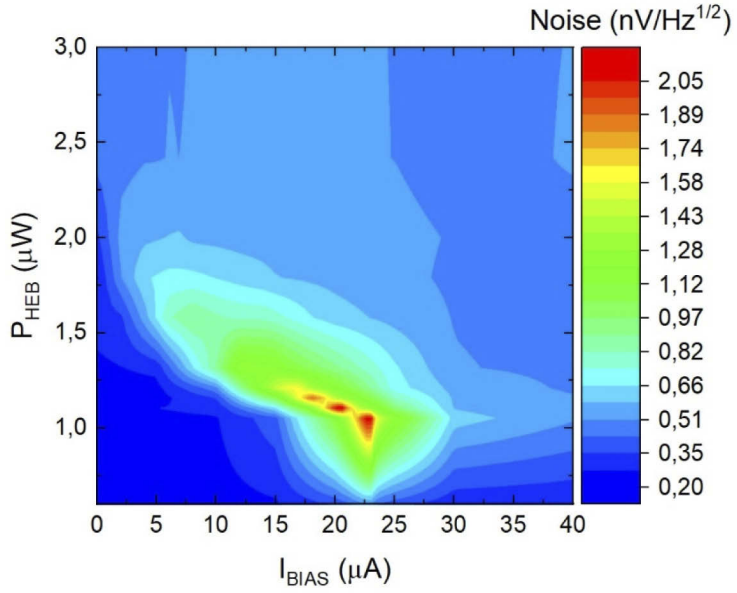

Fig. 5. Contour plot of the HEB voltage noise *Vn* measured at 90 MHz as a function of both local oscillator power P_{HEB} and bias current I_B. The voltage noise V_n is referred to the input of the LNA amplifier

In order to retrieve the clearance between shot noise and electrical noise, we have to estimate the parameters R_d, R and G from the IV characteristics of Fig. 2. The thermal conductivity G associates a power flow to a temperature change. By calculating the change of dissipated power by two isothermal IV characteristics for T approaching T_C (T_1=6.2K and T_2=6.5K of Fig. 2(a)), we retrieve:

$$G = \frac{P_1 - P_2}{T_1 - T_2} \approx 70\ nW/K \tag{7}$$

where $P_i = I_{Bi} \cdot V_{Bi}$, for i=1,2 are the dissipated powers calculated where R_d/R has a maximum (see Supplement 1). From the IV at P_{HEB}=1.11 μW (Fig. 2(b)), we retrieved $R_d \backsimeq 100$ Ω and $R \backsimeq 0$ Ω at $I_B = 20.5$ μA (see Supplement 1). By considering a responsivity of 8600 V/W and by computing the total electronic noise $NEP_{EL} = 47$ fW/ Hz$^{1/2}$, we estimate a light-independent

Optics EXPRESS

voltage noise V_{n-EL}=NEP_{EL}· Resp = 0.4 nV/ $Hz^{1/2}$, which is about a factor 5 smaller than the measured voltage noise V_n=2.21 nV/ $Hz^{1/2}$ (NEP_{tot}=260 fW/ $Hz^{1/2}$). Consequently, we can infer contribution of the shot noise equal to 2.17nV/ $Hz^{1/2}$ and retrieve a clearance value of 14.8 dBV.

This shot-noise level corresponds to an absorbed optical power of 0.25 μW (from Eq. (6)) and consequently an absorption efficiency η=22% of the total light inserted into the waveguide. The absorption efficiency can be decomposed in two independent contributes $\eta=\eta_I \cdot \eta_C$, where η_C accounts for the optical coupling efficiency meanwhile η_I describes the HEB internal efficiencies, as not all of the absorbed photons contribute to the output electrical signal. From the simulated optical coupling (Fig. 1(a)), we expect η_C=57% of the light absorbed in the HEB active area due to both light reflection at the waveguide end (due to a mismatch of effective refractive index at the interface between the waveguide and the substrate) and the small HEB surface, which is not large enough to absorb completely the coupled light. The internal efficiency is therefore η_I=39% and can be directly linked to the NbN material quality.

The classical definition of quantum efficiency employed for photodiodes is not suited to describe the HEB ability to measure light as to each absorbed photon corresponds a signal composed of several electrons. The inefficiencies of the HEB can instead be taken into account by the absorption efficiency η, whose value has to be maximized in order prevent any information loss in CV experiments. η_C can be maximized by using a mode converter at the waveguide end to avoid light reflection and by increasing the surface of the HEB. If we consider a HEB surface of 2×2μm^2, η_C would increase up to 82%. Another approach, that would not impact on the geometries of the HEB, consists in the use of photonic structures where the photon-material interaction is maximized. One way to achieve this is obtained by placing the HEB inside an optical cavity, for example. The internal efficiency η_I can instead be increased by optimizing the deposition parameters.

An important parameter used to characterize HEB mixers is the noise temperature [41] that is defined as

$$T_M = \frac{NEP_{tot}^2}{2\alpha k_B P_{HEB}} \tag{8}$$

where α defines the amount of absorbed power $P_{abs} = \alpha P_{HEB}$. By applying the isothermal method [29] at the IV characteristics of Fig. 2(b), we can estimate α≃18% (see Supplement 1) for the HEB in a quasi-normal state. Consequently, the noise temperature T_M = 11975 K is just 1.1 dB above the quantum noise limit temperature $T_Q = h\nu/k_B = 9275\ K$. The absorption coefficient α retrieved with the isothermal method is therefore in good agreement with the value of absorbed power retrieved from the measured shot noise.

5. Conclusion

Even though NbN SNSPDs have shown great performances in term of detection efficiency and technological compatibility with most of photonic platforms, their strong nonlinear response is not suited to detect linearly coherent beams due to a low saturation power. On the other side, HEBs have the advantage to share the same technological properties of NbN and they responds linearly to weak change of temperature caused by the absorption of higher-power light beam.

In this work, we reported the optical performances of a 1×1 μm^2 HEB integrated on a SOI photonic circuit operating in the telecom range. Even though HEB have been long used for optical detection at MIR and THz wavelength ranges, thanks to an optimal coupling and a reduced HEB dimensions we were able to measure the shot noise with just only 1.11 μW of pump power and 14.8 dBV clearance over electrical noise. Homodyne detectors with a NEP_{EL} as low as 47 fW/$Hz^{1/2}$, estimated for the integrated HEB, could be beneficial CW Quantum Communication protocols [42]. In addition, further optimization of both the optical coupling and NbN deposition, shot-noise limited HEB with unity quantum efficiency could be soon integrated together with SNSPDs on non-linear photonic platforms for an efficient generation

Optics EXPRESS

and characterization of complex non classical states of light within the same chip, enabling large-scale Quantum Information Processing with CV states.

Funding. H2020 Marie Skłodowska-Curie Actions (795923, ShaMROCk).

Acknowledgments. All authors thank Dr. A. Politi for helpful advice.

Disclosures. The authors declare no conflicts of interest.

Supplemental document. See Supplement 1 for supporting content.

References

1. D. T. Smithey, M. Beck, M. G. Raymer, and A. Faridani, "Measurement of the Wigner distribution and the density matrix of a light mode using optical homodyne tomography: Application to squeezed states and the vacuum," Phys. Rev. Lett. **70**(9), 1244–1247 (1993).
2. A. Zavatta, S. Viciani, and M. Bellini, "Quantum-to-classical transition with single-photon-added coherent states of light," Science **306**(5696), 660–662 (2004).
3. A. Ourjoumtsev, R. Tualle-Brouri, J. Laurat, and P. Grangier, "Generating optical Schrödinger kittens for quantum information processing SOM," Science **312**(5770), 83–86 (2006).
4. C. Weedbrook, S. Pirandola, R. García-Patrón, N. J. Cerf, T. C. Ralph, J. H. Shapiro, and S. Lloyd, "Gaussian quantum information," Rev. Mod. Phys. **84**(2), 621–669 (2012).
5. P. Jouguet, S. Kunz-Jacques, A. Leverrier, P. Grangier, and E. Diamanti, "Experimental demonstration of long-distance continuous-variable quantum key distribution," Nat. Photonics **7**(5), 378–381 (2013).
6. R. Schnabel, N. Mavalvala, D. E. McClelland, and P. K. Lam, "Quantum metrology for gravitational wave astronomy," Nat. Commun. **1**(1), 121 (2010).
7. W. Asavanant, Y. Shiozawa, S. Yokoyama, B. Charoensombutamon, H. Emura, R. N. Alexander, S. Takeda, J. ichi Yoshikawa, N. C. Menicucci, H. Yonezawa, and A. Furusawa, "Generation of time-domain-multiplexed two-dimensional cluster state," Science **366**(6463), 373–376 (2019).
8. J. L. O'Brien, A. Furusawa, and J. Vučković, "Photonic quantum technologies," Nat. Photonics **3**(12), 687–695 (2009).
9. G. Masada, K. Miyata, A. Politi, T. Hashimoto, J. L. O'Brien, and A. Furusawa, "Continuous-variable entanglement on a chip," Nat. Photonics **9**(5), 316–319 (2015).
10. F. Lenzini, J. Janousek, O. Thearle, M. Villa, B. Haylock, S. Kasture, L. Cui, H. P. Phan, D. V. Dao, H. Yonezawa, P. K. Lam, E. H. Huntington, and M. Lobino, "Integrated photonic platform for quantum information with continuous variables," Sci. Adv. **4**(12), eaat9331 (2018).
11. F. Raffaelli, G. Ferranti, D. H. Mahler, P. Sibson, J. E. Kennard, A. Santamato, G. Sinclair, D. Bonneau, M. G. Thompson, and J. C. F. Matthews, "A homodyne detector integrated onto a photonic chip for measuring quantum states and generating random numbers," Quantum Sci. Technol. **3**(2), 025003 (2018).
12. T. Kashiwazaki, N. Takanashi, T. Yamashima, T. Kazama, K. Enbutsu, R. Kasahara, T. Umeki, and A. Furusawa, "Continuous-wave 6-dB-squeezed light with 2.5-THz-bandwidth from single-mode PPLN waveguide," APL Photonics **5**(3), 036104 (2020).
13. M. E. Anderson, J. D. Bierlein, M. Beck, and M. G. Raymer, "Quadrature squeezing with ultrashort pulses in nonlinear-optical waveguides," Opt. Lett. **20**(6), 620–622 (1995).
14. F. Kaiser, B. Fedrici, A. Zavatta, V. D'Auria, and S. Tanzilli, "A fully guided-wave squeezing experiment for fiber quantum networks," Optica **3**(4), 362 (2016).
15. S. Yokoyama, R. Ukai, S. C. Armstrong, C. Sornphiphatphong, T. Kaji, S. Suzuki, J. Yoshikawa, H. Yonezawa, N. C. Menicucci, and A. Furusawa, "Ultra-large-scale continuous-variable cluster states multiplexed in the time domain," Nat. Photonics **7**(12), 982–986 (2013).
16. F. Mondain, T. Lunghi, A. Zavatta, E. Gouzien, F. Doutre, M. De Micheli, S. Tanzilli, and V. D'Auria, "Chip-based squeezing at a telecom wavelength," Photonics Res. **7**(7), A36 (2019).
17. M. Pysher, R. Bloomer, C. M. Kaleva, T. D. Roberts, P. Battle, and O. Pfister, "Broadband amplitude squeezing in a periodically poled KTiOPO_4 waveguide," Opt. Lett. **34**(3), 256 (2009).
18. R. Cernansky and A. Politi, "Nanophotonic source of quadrature squeezing via self-phase modulation," APL Photonics **5**(10), 101303 (2020).
19. Z. Vernon, N. Quesada, M. Liscidini, B. Morrison, M. Menotti, K. Tan, and J. E. Sipe, "Scalable Squeezed-Light Source for Continuous-Variable Quantum Sampling," Phys. Rev. Appl. **12**(6), 064024 (2019).
20. R. Kumar, E. Barrios, A. Macrae, E. Cairns, E. H. Huntington, and A. I. Lvovsky, "Versatile wideband balanced detector for quantum optical homodyne tomography," Opt. Commun. **285**(24), 5259–5267 (2012).
21. D. Ahn, C. Hong, J. Liu, W. Giziewicz, M. Beals, L. C. Kimerling, J. Michel, J. Chen, and F. X. Kärtner, "High performance, waveguide integrated Ge photodetectors," Opt. Express **15**(7), 3916 (2007).
22. Z. Sheng, L. Liu, J. Brouckaert, S. He, and D. Van Thourhout, "InGaAs PIN photodetectors integrated on silicon-on-insulator waveguides," Opt. Express **18**(2), 1756 (2010).
23. J. E. Muench, A. Ruocco, M. A. Giambra, V. Miseikis, D. Zhang, J. Wang, H. F. Y. Watson, G. C. Park, S. Akhavan, V. Sorianello, M. Midrio, A. Tomadin, C. Coletti, M. Romagnoli, A. C. Ferrari, and I. Goykhman, "Waveguide-Integrated, Plasmonic Enhanced Graphene Photodetectors," Nano Lett. **19**(11), 7632–7644 (2019).

Optics EXPRESS

24. N. Flöry, P. Ma, Y. Salamin, A. Emboras, T. Taniguchi, K. Watanabe, J. Leuthold, and L. Novotny, "Waveguide-integrated van der Waals heterostructure photodetector at telecom wavelengths with high speed and high responsivity," Nat. Nanotechnol. **15**(2), 118–124 (2020).
25. A. Shurakov, Y. Lobanov, and G. Goltsman, "Superconducting hot-electron bolometer: from the discovery of hot-electron phenomena to practical applications," Supercond. Sci. Technol. **29**(2), 023001 (2016).
26. Y. Ren, D. Zhang, Z. Wang, K. Zhou, J. Zhong, D. Liu, W. Miao, W. Zhang, and S. Shi, "Quantum cascade laser based, fiber coupled demultiplexed mid-infrared local oscillator for cryogenic applications," Appl. Phys. Lett. **116**(13), 131108 (2020).
27. S. Seliverstov, S. Maslennikov, S. Ryabchun, M. Finkel, T. M. Klapwijk, N. Kaurova, Y. Vachtomin, K. Smirnov, B. Voronov, and G. Goltsman, "Fast and sensitive terahertz direct detector based on superconducting antenna-coupled hot electron bolometer," IEEE Trans. Appl. Supercond. **25**(3), 1 (2014).
28. S. Cibella, P. Carelli, M. G. Castellano, F. Chiarello, A. Gaggero, E. Giovine, G. Scalari, G. Torrioli, and R. Leoni, "A metamaterial-coupled hot-electron-bolometer working at THz frequencies," in *Terahertz, RF, Millimeter, and Submillimeter-Wave Technology and Applications X*, L. P. Sadwick and T. Yang, eds. (SPIE, 2017), Vol. 10103, p. 101031M.
29. Y. Lobanov, M. Shcherbatenko, M. Finkel, S. Maslennikov, A. Semenov, B. M. Voronov, A. V. Rodin, T. M. Klapwijk, and G. N. Gol'tsman, "NbN hot-electron-bolometer mixer for operation in the near-IR frequency range," IEEE Trans. Appl. Supercond. **25**(3), 1–4 (2015).
30. Y. Lobanov, M. Shcherbatenko, A. Shurakov, A. V. Rodin, A. Klimchuk, A. I. Nadezhdinsky, S. Maslennikov, P. Larionov, M. Finkel, A. Semenov, A. A. Verevkin, B. M. Voronov, Y. Ponurovsky, T. M. Klapwijk, and G. N. Gol'tsman, "Heterodyne detection at near-infrared wavelengths with a superconducting NbN hot-electron bolometer mixer," Opt. Lett. **39**(6), 1429 (2014).
31. W. H. P. Pernice, C. Schuck, O. Minaeva, M. Li, G. N. Goltsman, A. V. Sergienko, and H. X. Tang, "High-speed and high-efficiency travelling wave single-photon detectors embedded in nanophotonic circuits," Nat. Commun. **3**(1), 1325 (2012).
32. A. Gaggero, F. Martini, F. Mattioli, F. Chiarello, R. Cernansky, A. Politi, and R. Leoni, "Amplitude-multiplexed readout of single photon detectors based on superconducting nanowires," Optica **6**(6), 823 (2019).
33. F. Martini, A. Gaggero, F. Mattioli, and R. Leoni, "Single photon detection with superconducting nanowires on crystalline silicon carbide," Opt. Express **27**(21), 29669 (2019).
34. A. Al Sayem, R. Cheng, S. Wang, and H. X. Tang, "Lithium-Niobate-on-Insulator Waveguide-Integrated Superconducting Nanowire Single-Photon Detectors," (2019).
35. R. N. Alexander, S. Yokoyama, A. Furusawa, and N. C. Menicucci, "Universal quantum computation with temporal-mode bilayer square lattices," Phys. Rev. A **97**(3), 032302 (2018).
36. . "CITLF3 - Cosmic Microwave Technology Inc," https://www.cosmicmicrowavetechnology.com/citlf3.
37. T. M. Klapwijk and A. V. Semenov, "Engineering Physics of Superconducting Hot-Electron Bolometer Mixers," IEEE Trans. Terahertz Sci. Technol. **7**(6), 627–648 (2017).
38. A. Yariv and P. Yeh, *Photonics: Optical Electronics in Modern Communications (the Oxford Series in Electrical and Computer Engineering)* (Oxford University, Inc., 2006).
39. J. C. Mather, "Bolometer noise: nonequilibrium theory," Appl. Opt. **21**(6), 1125 (1982).
40. M. Galeazzi, "Fundamental noise processes in TES devices," IEEE Trans. Appl. Supercond. **21**(3), 267–271 (2011).
41. B. S. Karasik and A. I. Elantiev, "Noise temperature limit of a superconducting hot-electron bolometer mixer," Appl. Phys. Lett. **68**(6), 853–855 (1996).
42. S. Fossier, E. Diamanti, T. Debuisschert, A. Villing, R. Tualle-Brouri, and P. Grangier, "Field test of a continuous-variable quantum key distribution prototype," New J. Phys. **11**(4), 045023 (2009).